Adaptive In-Sensor Computing for Enhanced Feature Perception and Broadband Image Restoration

He Shao, Weijun Wang, Yuxuan Zhang, Boxiang Gao, Chunsheng Jiang, Yezhan Li, Pengshan Xie, Yan Yan, Yi Shen, Zenghui Wu, Ruiheng Wang, Yu Ji, Haifeng Ling,* Wei Huang,* and Johnny C. Ho*

Traditional imaging systems struggle in weak or complex lighting environments due to their fixed spectral responses, resulting in spectral mismatches and degraded image quality. To address these challenges, a bioinspired adaptive broadband image sensor is developed. This innovative sensor leverages a meticulously designed type-I heterojunction alignment of 0D perovskite quantum dots (PQDs) and 2D black phosphorus (BP). This configuration enables efficient carrier injection control and advanced computing capabilities within an integrated phototransistor array. The sensor's unique responses to both visible and infrared (IR) light facilitate selective enhancement and precise feature extraction under varying lighting conditions. Furthermore, it supports real-time convolution and image restoration within a convolutional autoencoder (CAE) network, effectively countering image degradation by capturing spectral features. Remarkably, the hardware responsivity weights perform comparably to software-trained weights, achieving an image restoration accuracy of over 85%. This approach offers a robust and versatile solution for machine vision applications that demand precise and adaptive imaging in dynamic lighting environments.
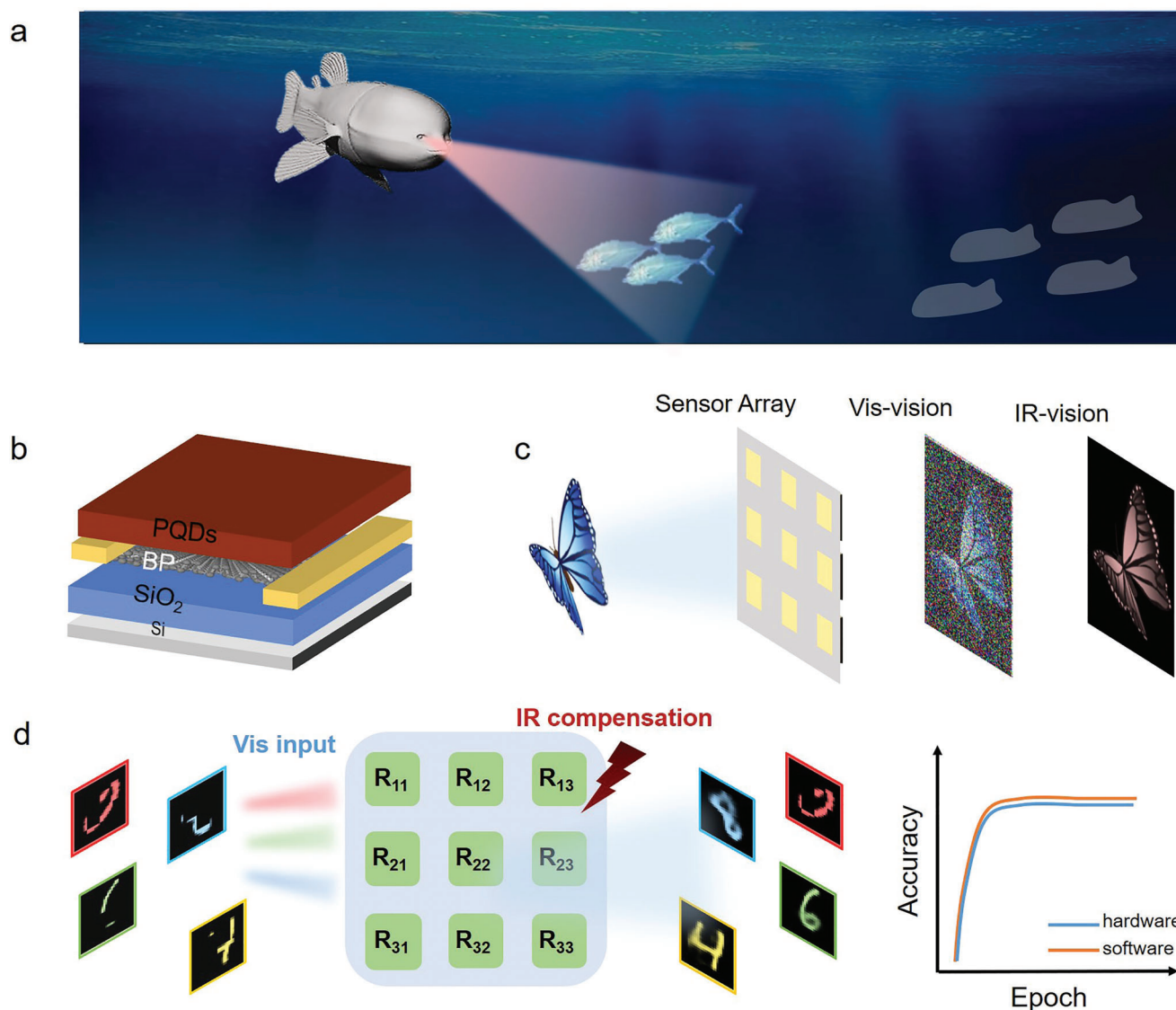
H. Shao, W. Wang, Y. Zhang, B. Gao, C. Jiang, Y. Li, P. Xie, Y. Yan, Y. Shen, Z. Wu, J. C. Ho
Department of Materials Science and Engineering
City University of Hong Kong
Hong Kong SAR 999077, China
E-mail: johnnyho@cityu.edu.hk
R. Wang, Y. Ji, H. Ling, W. Huang
State Key Laboratory of Organic Electronics and Information Displays &
Institute of Advanced Materials (IAM)
Nanjing University of Posts & Telecommunications (NJUPT)
Nanjing 210023, China
E-mail: iamhfling@njupt.edu.cn; vc@nwpu.edu.cn
J. C. Ho
State Key Laboratory of Terahertz and Millimeter Waves
City University of Hong Kong
Hong Kong SAR 999077, China
J. C. Ho
Institute for Materials Chemistry and Engineering
Kyushu University
Fukuoka 816–8580, Japan

1. Introduction

Traditional imaging systems struggle to effectively capture and process visual information in many real-world scenarios, especially those involving complex lighting conditions.[1,2] These challenges are particularly pronounced in weak or fluctuating light environments, where light intensity and spectral composition variations can obscure crucial details in the target scene.[3,4] Conventional complementary metal-oxide-semiconductor (CMOS) sensors exhibit significant limitations in complex lighting environments, primarily due to their narrow and fixed spectral response range, which is typically confined to the RGB (visible) spectrum.[5,6] This fixed response restricts their adaptability to varying environmental spectra, resulting in compromised image quality under weak-light, high-backlight, or multispectral conditions.[7,8] Moreover, CMOS sensors rely on subsequent external image processing to correct spectral discrepancies, limiting their capacity for real-time image enhancement. Therefore, there is a pressing need to explore more advanced image sensing and processing technologies that adapt to dynamic lighting conditions, enhancing visual perception and data integrity.[9,10]

Recent advancements in light intensity adaptation offer promising solutions for capturing accurate images under diverse high-dynamic-range illumination conditions. By equipping vision sensors with the ability to adapt to the dynamic spectra of their environment, these systems significantly improve their capacities to perceive and interpret visual information associated with specific spectral signatures.[11] In addition, spectral adaptive vision sensors have been designed to accommodate spectral shifts across different environmental contexts.[12] Nature provides valuable insights for developing comprehensive machine vision capabilities, as certain organisms have evolved specialized visual mechanisms to respond to changes in spectral conditions.[13] A notable example is the deep-sea fish Macropinna, which has a transparent head and tubular eyes that detect active prey while avoiding environmental obstacles (**Figure 1a**).[14] This adaptation allows it to thrive in the deep

**ADVANCED
SCIENCE NEWS**

www.advancedsciencenews.com

**ADVANCED
MATERIALS**

www.advmat.de

Figure 1. a) Macropinna's distinctive visual ability allows it to eliminate background interference and effectively capture prey, even in the deep sea's challenging weak/complex lighting conditions. b) Schematic diagram of the PQDs/BP phototransistor. c) The object capture through the phototransistor array with vis-model and IR-model. d) The phototransistor array restores damaged images by compensating with IR light.

ocean with scarce light by detecting faint bioluminescent signals and adjusting its vision to the specific spectral conditions. The spectral adaptability demonstrated by Macropinna serves as an insightful model for developing advanced image processing systems, potentially enhancing their performance in complex lighting conditions.[15–17]

In this work, we have designed a bioinspired adaptive broadband image sensor engineered from heterojunctions that incorporate 0D perovskite quantum dots (PQDs) and few-layer 2D black phosphorus (BP) nanoflakes (Figure 1b). The CsPb(Br/I)$_3$ PQDs facilitate tunable bandgaps by modulating the Br/I ratio, thereby optimizing absorption properties across a broad spectral range.[18] Inspired by the structural design and optoelectronic properties of historic organic molecular and polymer-based transistors, heterojunctions formed by organic photosensitive

materials and inorganic 2D materials offer diverse tunability in photoresponse. This hybrid approach enables enhanced control over light absorption and carrier dynamics, paving the way for advanced applications in optoelectronics.[19–22] This novel 0D/2D type-I heterojunction system demonstrates unique responses to both visible and infrared (IR) light, allowing the sensor array to selectively enhance and accurately extract image features under low or complex lighting conditions (Figure 1c). The dual-mode response is particularly advantageous for applications that require reliable image capture in challenging lighting environments. Moreover, this capability allows the device to function as a convolutional kernel within a convolutional autoencoder (CAE) network, facilitating in-sensor computing for real-time image processing and restoration. The precisely calibrated IR response enables dynamic spectral adjustments,

**ADVANCED
SCIENCE NEWS**

www.advancedsciencenews.com

**ADVANCED
MATERIALS**

www.advmat.de

effectively restoring damaged images by capturing the spectral features of the target and mitigating image quality degradation caused by spectral mismatches (Figure 1d). Notably, within the CAE network, the hardware responsivity weights achieve performance comparable to software-trained weights, restoring lost regions and maintaining a recognition accuracy of over 85%. This approach offers a robust and versatile solution for critical applications that demand precise and adaptive imaging.

2. Results and Discussion

2.1. Design of Phototransistors with Low-Dimensional Heterojunctions

The air-stable $CsPb(Br/I)_3$ perovskite quantum dots (PQDs) were synthesized using a hot injection method.[23] They were then passivated with lecithin to enhance their ambient stability and sensitivity to visible light.[24–26] The synthetic process of lecithin-modified $CsPb(Br/I)_3$ PQDs is illustrated in Figure S1 (Supporting Information). The Fourier-transform infrared spectroscopy (FTIR) results in Figure S2 (Supporting Information) demonstrate that the characteristic peaks of lecithin at 3350 and 1062 cm^{-1} are present on the surface of the modified PQDs, indicating the successful modification of lecithin on the PQD surface.[27] The addition of lecithin during the synthesis process significantly improves the ambient stability of the $CsPb(Br/I)_3$ PQDs, allowing them to retain their cubic crystal structure even after months of storage under ambient conditions, as supported by TEM and XRD results (Figures S3 and S4, Supporting Information).[28,29]

Furthermore, given the suitable bandgap and high hole mobility, a few-layer BP nanoflake was utilized to absorb IR light and facilitate carrier transport. To shed light on the device structure, cross-sectional scanning transmission electron microscopy (STEM) and energy-dispersive X-ray spectroscopy (EDS) mapping were conducted on the mixed-dimensional 0D/2D device (**Figure 2a**). A clear heterostructure interface was observed in the EDS mapping result, precisely showing the spatial distribution of various elements at the interface, confirming the uniformity and purity of the materials involved. As shown in Figures 2b,c, the exfoliated 2D BP nanoflake shows a smooth surface morphology, along with the characteristic Raman peaks and uniform signal distribution of Raman mapping, indicating successful preservation of structural integrity and material quality.[30,31] The optical image in Figure 2d clearly shows the phototransistor based on the BP channel. Here, PQDs serve as the visible light absorption layer, while BP dominantly interacts with IR light and is responsible for carrier transport. The high-quality lecithin-modified PQDs layer is directly witnessed by the bright and uniform red emission across the entire device when irradiated by 365 nm UV light. The photoluminescence quantum yield (PLQY) of PQD film maintained a bright red emission with a high PLQY of 76% after three days under ambient conditions, indicating exceptional stability (Figure S5, Supporting Information). Even after three months of storage in ambient, the intact optical properties of lecithin-modified PQDs could also be detected by absorption spectra and photoluminescence (PL), further highlighting the passivation function of lecithin ligand on PQDs (Figures S6 and S7, Supporting Information).[32,33]

As the transfer characteristics (I_{DS}-V_{GS}) and output characteristics are shown in Figures 2e and S8 (Supporting Information), the PQDs/BP device demonstrates a typical p-type transport behavior with an on/off current ratio of 10^3. The V_t and mobility (μ) were calculated to be 26.2 V and 225.2 cm^2 V^{-1} s^{-1}, indicating the device's highly efficient charge transport (Figure S9, Supporting Information). Figure S10 (Supporting Information) illustrates the transfer characteristics of devices with varying BP and PQD layer thicknesses, showing that an increased BP thickness results in a higher off-state current and a reduced on/off ratio. In contrast, a thicker PQD layer further elevates the off-state current. These findings underscore the significant influence of BP nanoflake and PQD layer thickness on device-switching behaviors. Subsequently, the device's transfer characteristics variation under different light wavelength conditions is investigated, as shown in Figure 2e. When exposed to 1550 nm light, compared to the dark condition, the transfer curve of the PQDs/BP phototransistor shows a positive shift and a higher photocurrent (reading at $V_{GS} = 10$ V), indicating a positive photoresponse.[34] Conversely, under visible light (including 450, 532, and 635 nm), the transfer curve shows a negative shift and a lower drain current, suggesting a negative photoresponse. Figure 2f illustrates the related charge transport mechanism at different wavelengths. When exposed to visible light, electrons are photo-generated and transferred from PQDs to BP due to the high visible absorption efficiency of PQDs. A detailed drift-diffusion model was developed to examine the effects of defect states on the phototransistor performance. The carrier mobility, absorption coefficient, and defect-induced recombination mechanisms were integrated to analyze the device behavior. It reveals that the BP interface with a high defect density substantially increases the voltage.[35] The interface trap density was estimated to be 1.2×10^{13} cm^{-2} eV^{-1} (Figure S11, Supporting Information). This effect arises as defect states capture charge carriers, generating interface trap charges that shift the transfer characteristics and necessitate a higher supply voltage.

The ultraviolet photoelectron spectroscopy (UPS) measurements (Figure S12, Supporting Information) further confirmed the electronic structure of the modified PQDs, revealing a valence band maximum of -5.76 eV and a conduction band minimum of -3.66 eV, thereby providing insight into their energy levels. Meanwhile, the holes generated in the PQDs are blocked by a barrier that prevents them from entering the BP. The transferred electrons recombine with holes in BP, thus reducing the current in the channel. These features make the mixed-dimensional device a promising candidate for in-sensor computing with polarity-tunable photoresponse. Conversely, when exposed to 1550 nm light, excitons are only generated within the BP nanoflake because the photon energy is lower than the bandgap of PQDs, increasing hole concentration and photocurrent in the channel.[36,37]

2.2. Bidirectional Photoresponse Characteristics of Phototransistor Arrays

Figure 3a exhibits the photoresponse of the PQDs/BP phototransistor under 450 nm light pulses, exhibiting a negative photoresponse analogous to the inhibitory postsynaptic current (IPSC)
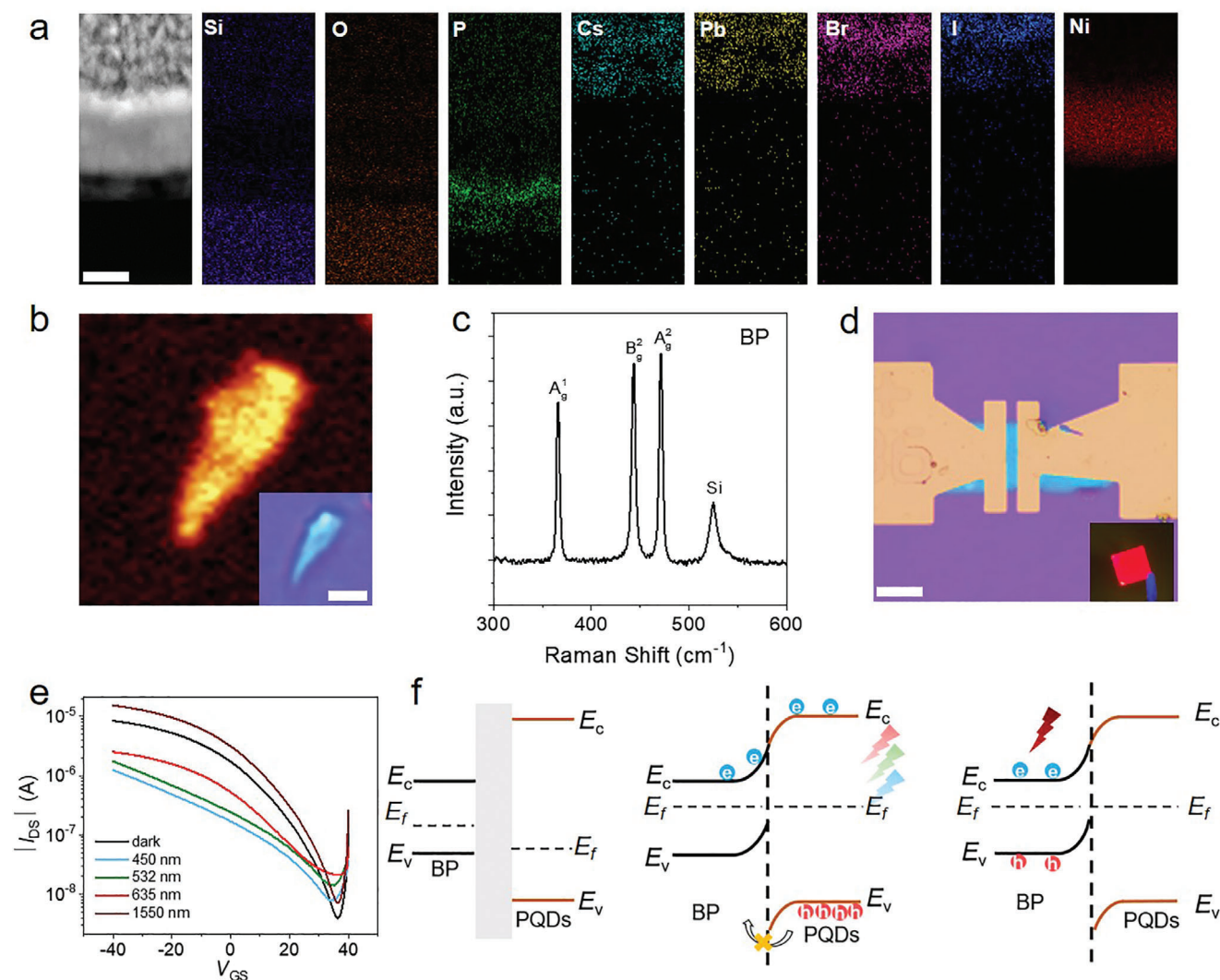
Figure 2. a) STEM image and EDS mapping of the PQDs/BP phototransistor. The scale bar is 20 nm. b,c) Raman mapping and spectra of the exfoliated BP nanoflake. The inset shows the optical image; the scale bar is 5 μm. d) Optical image of the PQDs/BP phototransistor; the scale bar is 5 μm. The inset shows the graph under 365 nm light. e) Transfer curves measured under dark and light illumination with different wavelengths. f) Operating mechanism of the PQDs/BP phototransistor under different light conditions.

observed in biological synapses.[37–39] The long-term depression (LTD) behavior of the PQDs/BP phototransistor is demonstrated by applying 100 consecutive optical spikes, each with a duration of t_d = 0.1 s, as shown in Figure 3b. Notably, as the spike interval (Δt) decreases from 0.5 to 0.1 s, the photocurrent suppression intensifies, with the recovery time extending to several hundred seconds. This LTD synaptic plasticity, a characteristic feature of biological neural networks, is triggered by exposure to blue, green, and red lights, enabled by the visible absorption properties of PQDs. Given the higher absorption efficiency of PQDs at shorter wavelengths, the device's inhibitory behavior is more pronounced under blue light stimulation than red light, as depicted in Figure 3c. Figure S13 (Supporting Information) presents a 2D color mapping of the device current across different wavelengths and light powers. Similarly, as the pulse number and light power increase, the photocurrent exhibits a steady degradation across all visible light wavelengths. The controllable decrease in cur-

rent with increasing pulse count and light intensity demonstrates that the system's performance is both reliable and adaptable, enhancing its suitability for practical dynamic and adaptive systems. Subsequently, the device's response characteristics will be evaluated following extended exposure to various light wavelengths. After sequential 6-h exposures to 450, 532, and 635 nm lights, the device's photoresponse characteristics were remeasured, as shown in Figure S14 (Supporting Information). The results reveal a gradual decrease in photocurrent after prolonged illumination. Despite this reduction, the device maintains a consistent response trend across three wavelengths. The observed decrease in photocurrent is primarily attributed to the degradation of PQDs under extended light exposure.[40] This degradation affects the charge generation and transport, leading to a lower photocurrent over time.

Figure 3d shows the positive photoresponse of the device under 1550 nm irradiation with varying light intensities. The

ADVANCED
SCIENCE NEWS

www.advancedsciencenews.com

**ADVANCED
MATERIALS**

www.advmat.de
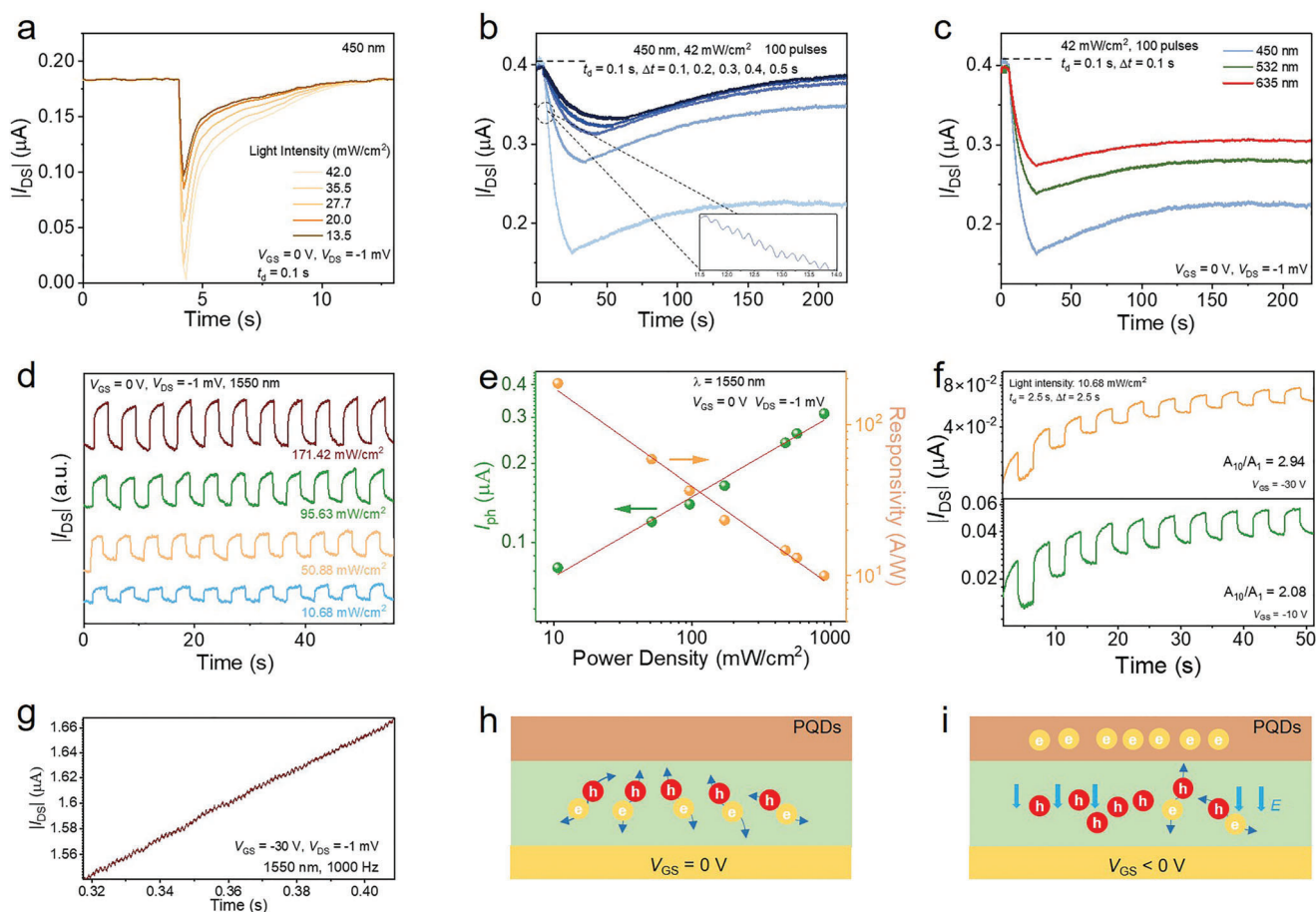
Figure 3. a) Photoresponse of PQDs/BP phototransistors under a single 450 nm light pulse with different intensities. b) Photoresponse of PQDs/BP phototransistors under 100 consecutive 450 nm light pulses. c) Photoresponse of the device under 100 consecutive light pulses with different wavelengths. d) *I*-*t* curves of the device in response to consecutive 1550 nm light pulses with different light intensities. e) Photocurrent and responsivity as a function of light intensities. f) *I*-*t* curves of the device in response to 1550 nm light pulses with V_{GS} of −30 V and −10 V. g) *I*-*t* curve of the device in response to 1550 nm light pulses chopped at 1000 Hz. h, i)The carrier transfer process of the device under 1550 nm illumination at V_{GS} of (h) 0 V and (i) −30 V.

temporal photoresponse of the device was investigated under 1550 and 450 nm light pulses. As shown in Figure S15a (Supporting Information), the rise and decay times for 1550 nm illumination were determined to be 14 and 135 ms, respectively. For the 450 nm light pulse response, the rise and decay times were measured at 80 ms and 3.3 s, as shown in Figure S15b (Supporting Information). This combination of rapid response and slow decay presents potential for modulating the synaptic behavior. Compared to conventional single-layer transistor devices, the slower response speed in this device is attributed to charge trapping at the heterojunction interface. To investigate this further, we conducted control experiments with a BP-based phototransistor without PQDs. As shown in Figure S16 (Supporting Information), the measured rise time was ≈230 μs, and the decay time was ≈340 μs, demonstrating an ultrafast response compared to PQDs/BP phototransistors. These results confirm that the QD layer introduces additional carrier trapping or recombination processes that extend the response time to 1550 nm light. The photocurrent as a function of light intensity shows a linear relationship (Figure 3e), suggesting a typical photoresponse

behavior of solid-state semiconductors.[41] Without gate voltage bias, the optimized responsivity is calculated to be ≈100 A W^{-1}. Considering the IR photon energy is lower than the bandgap of PQDs, BP dominantly interacts with IR light and is responsible for IR photoresponse in this work. By manipulating the band alignment of PQDs/BP phototransistors, their positive photoresponse can be modulated by gate voltages. The gate-dependent current response was further investigated in Figure S17 (Supporting Information). As the gate voltage varies from 0 to −30 V, the current response increases progressively, demonstrating effective control of charge transfer between PQDs and BP by the gate voltage. Continuous current responses at different gate voltages are similarly depicted in Figure 3f. After ten consecutive pulses, the current increase ratio (A_{10}/A_1) is 2.94 and 2.08 for gate voltages of −30 and −10 V, respectively. This positive photoconductance behavior simulates excitatory postsynaptic current (EPSC) and paired-pulse facilitation (PPF) in Figure S18 (Supporting Information), akin to biological synapses.[42,43] The PPF properties of PQDs/BP phototransistors were explored by applying pairs of 1550 nm optical spikes with a duration of 0.1 s and

**ADVANCED
SCIENCE NEWS**

www.advancedsciencenews.com

**ADVANCED
MATERIALS**

www.advmat.de

intervals ranging from 0.05 to 2 s. The PPF index is calculated as the ratio of EPSC amplitudes induced by the second (A_2) and first (A_1) presynaptic pulses (PPF index = $A_2/A_1 \times 100\%$).[44] A PPF index of ≈120% was achieved when the interval duration was 50 ms.

The photoresponse under high switching frequency was also evaluated, as illustrated in Figure 3g, using continuous light pulses modulated at 1000 Hz. The results demonstrate the device's ability to maintain distinct consecutive conductive states that steadily increase over time. The device's capability to handle high-frequency light pulses ensures it can effectively capture and interpret fast-changing visual information. It is well-suited for advanced machine vision systems that demand both speed and accuracy.[45] Moreover, the positive response behavior under different gate voltages is further explained in Figure 3h. When the gate voltage is 0, the IR light triggers the separation of electron-hole pairs in BP, which rapidly recombine after turning off, exhibiting a fast switching behavior. Under a negative gate voltage, the generated electric field drives electrons from BP into PQDs, and these transferred electrons act as a floating gate to maintain the BP channel conductance at a relatively high level (Figure 3i).

2.3. Feature Recognition of Phototransistor Arrays in Complex Lighting Environments

Traditional imaging systems face difficulties in deep-sea scenarios due to weak light conditions and light scattering, which hinder the accurate identification of marine life. These challenges underscore the limitations of conventional imaging methods that rely heavily on visible light and often fail to deliver precise and reliable results in murky underwater environments.[11,46] To address these issues, **Figure 4a** demonstrates an IR-sensitive imaging technology that enhances the detection and identification of underwater prey by utilizing the IR light. This capability significantly improves over traditional methods, offering greater visibility and accuracy in deep-sea imaging. Figure 4b illustrates a schematic of the application scenario for spectrum-adapted vision sensors. These sensors are engineered to operate across a broad range of wavelengths, enabling them to adapt to various environmental conditions. This adaptability is particularly beneficial in deep-sea exploration and other complex environments where traditional visible light imaging is insufficient. These vision sensors provide a robust solution for improving image clarity and detection accuracy by optimizing the sensor response to specific spectral ranges. As shown in Figure S19 (Supporting Information), a 3 × 3 phototransistor array was constructed for the compelling image sensor. After stimulation with a single light pulse of 450 and 1550 nm, the device array obtained reconfigurable positive and negative photoresponses.

Figure 4c shows the cumulative current measurements for progressive multilevel states under periodic optical pulses with 0.1 s intervals. The distinct photoresponses under different wavelengths were also demonstrated, with 450 nm irradiation represented by the blue line and 1550 nm irradiation represented by the red line. This wavelength-dependent sensitivity highlights its capability to adapt to different light conditions. Figure 4d shows the normalized cumulative photocurrent along with its linear fitting. The linearity of the response is essential for ensuring reli-

able performance and consistent results across different wavelengths. Figure S20 (Supporting Information) shows a similar trend in the current response under multiple green and red light pulses, showing distinct multi-stage variations. When 20 light pulses are applied, each current value reveals an apparent linear increase as the pulse number rises. This predictable behavior as a function of pulses is essential for applications requiring precise signal interpretation. Figures 4e and S21 (Supporting Information) provide a detailed analysis of the differences in positive and negative responses to IR and visible lights across 20 independent states. These results emphasize the sensor's accuracy in distinguishing between different signal levels, which is essential for accurate image detection and recognition.

The applications of the phototransistor array for image detection are demonstrated in Figure 4f, which shows the array's performance in both visible (vis-mode) and infrared (IR-mode) modes. Notably, the IR mode performs better in filtering RGB noise, making it more effective in complex light environments. This enhancement in noise reduction is critical for improving image clarity and recognition accuracy, particularly in challenging conditions where traditional imaging methods may struggle. Figure 4g exhibits the impact of RGB noise filtering using the phototransistor array in the IR mode on image recognition accuracy. Images affected by RGB noise achieve a recognition accuracy of only 15% when processed through an artificial neural network (ANN). However, after applying noise filtering, the recognition accuracy dramatically improves to 98.7%. This significant increase in accuracy underscores the advantages of integrating IR-sensitive phototransistor arrays into image processing systems. Such enhancements are particularly beneficial for applications that require precise image recognition in challenging conditions, such as autonomous vehicles, surveillance systems, medical diagnostics, and industrial manufacturing.

2.4. Infrared Compensation for Adaptive Broadband Damaged Image Restoration

Under weak and complex lighting conditions, such as overexposure or insufficient illumination, the imaging process often suffers from blurriness or missing details, significantly impacting the quality of visual information. Effective image restoration is essential for many machine vision and data preservation applications. However, traditional image sensors, primarily based on CMOS technology, face limitations in accurately and efficiently restoring lost image features due to their physically separated optoelectronic components, which hinder their ability to capture the spatial correlations necessary for precise restoration.[47,48] In contrast, the integrated CAE network enhances relevant image information, enabling more accurate and efficient restoration of damaged images. **Figure 5a** illustrates the compression and decompression processes within the CAE network. The CAE initially extracts local image features through convolutional operations. The encoder compresses this information into a lower-dimensional latent space, preserving essential features while reducing data dimensionality. The decoder then restores the original image from the compressed features (Figure S22, Supporting Information). By leveraging the CAE's specialized

**ADVANCED
SCIENCE NEWS**

www.advancedsciencenews.com

**ADVANCED
MATERIALS**

www.advmat.de
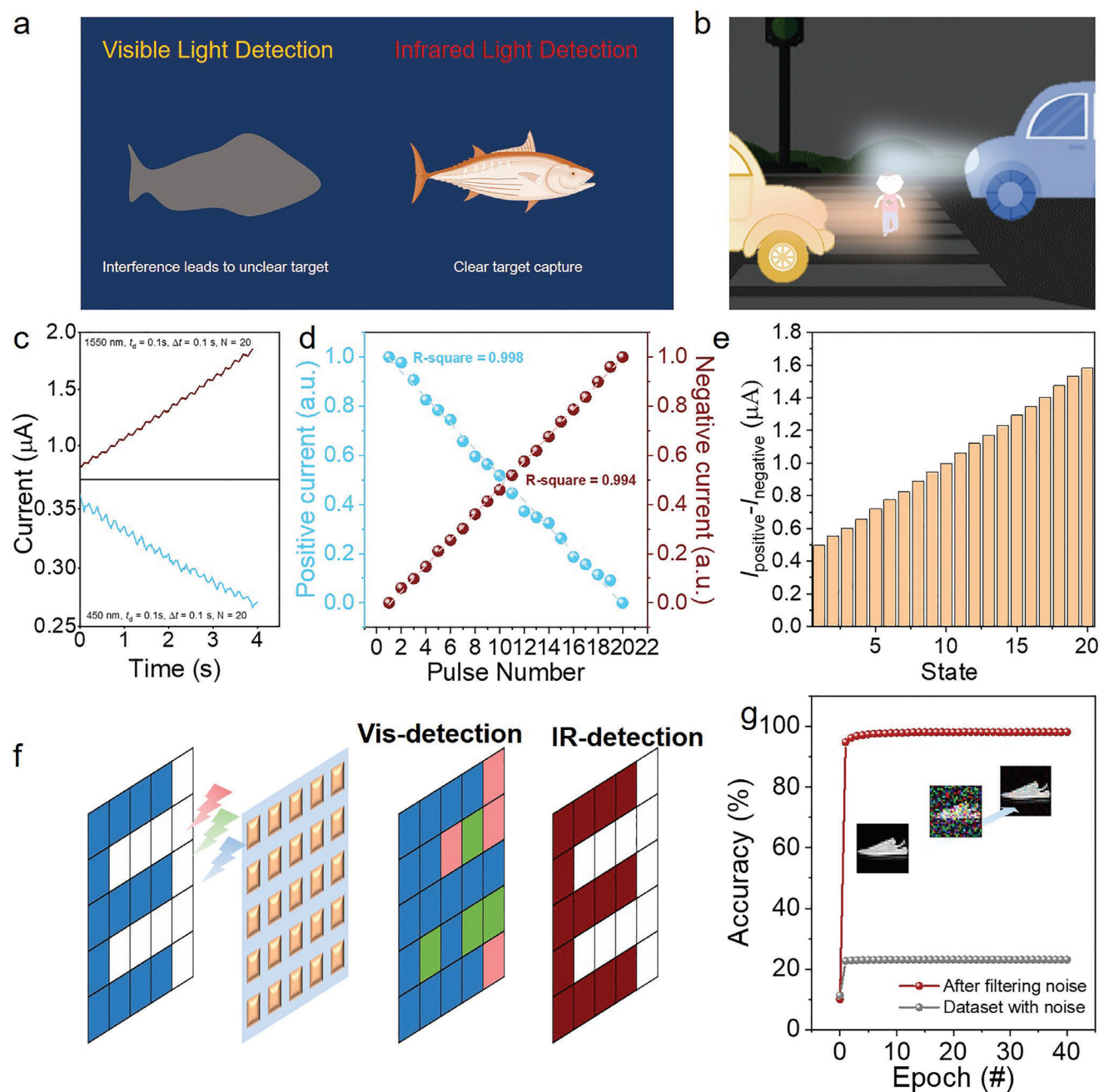
Figure 4. a) Traditional imaging systems struggling to identify marine life in the deep sea due to low light conditions and light scattering, and the IR-sensitive imaging technology effectively detecting and identifying prey in murky underwater environments. b) Schematic of the application scenario of the spectra-adapted vision sensors. c) Cumulative current for progressive multilevel states under periodic 0.1 s optical pulses with 0.1 s intervals; the blue line indicates 450 nm irradiation, while the red line indicates 1550 nm irradiation. d) Extracted normalized cumulative photocurrent under successive optical pulses with 450 and 1550 nm and the linear fitting. e) The difference between positive current with 1550 nm stimulation and negative current with 450 nm stimulation under 20 independent states. f) The image detection through a phototransistor array with vis-model and IR-model. g) Image recognition accuracy after RGB noise filtering using a phototransistor array with the IR mode.

architecture for unsupervised image restoration, we can achieve a more adaptive and efficient restoration process, underscoring its importance as an ideal choice for our sensor-integrated approach in complex lighting scenarios.

For image perception and parallel processing, the phototransistor array simultaneously receives image pixel information and performs convolution operations within the CAE network. Our device exhibits a unique bidirectional photoresponse to both visible and IR lights. Thus, when visible image data is damaged, the array utilizes IR light compensation to adaptively restore images across different colors (Figure 5b). The response weight sequences at 1550 and 450 nm were extracted (see Tables S1

ADVANCED
SCIENCE NEWS

www.advancedsciencenews.com

**ADVANCED
MATERIALS**

www.advmat.de
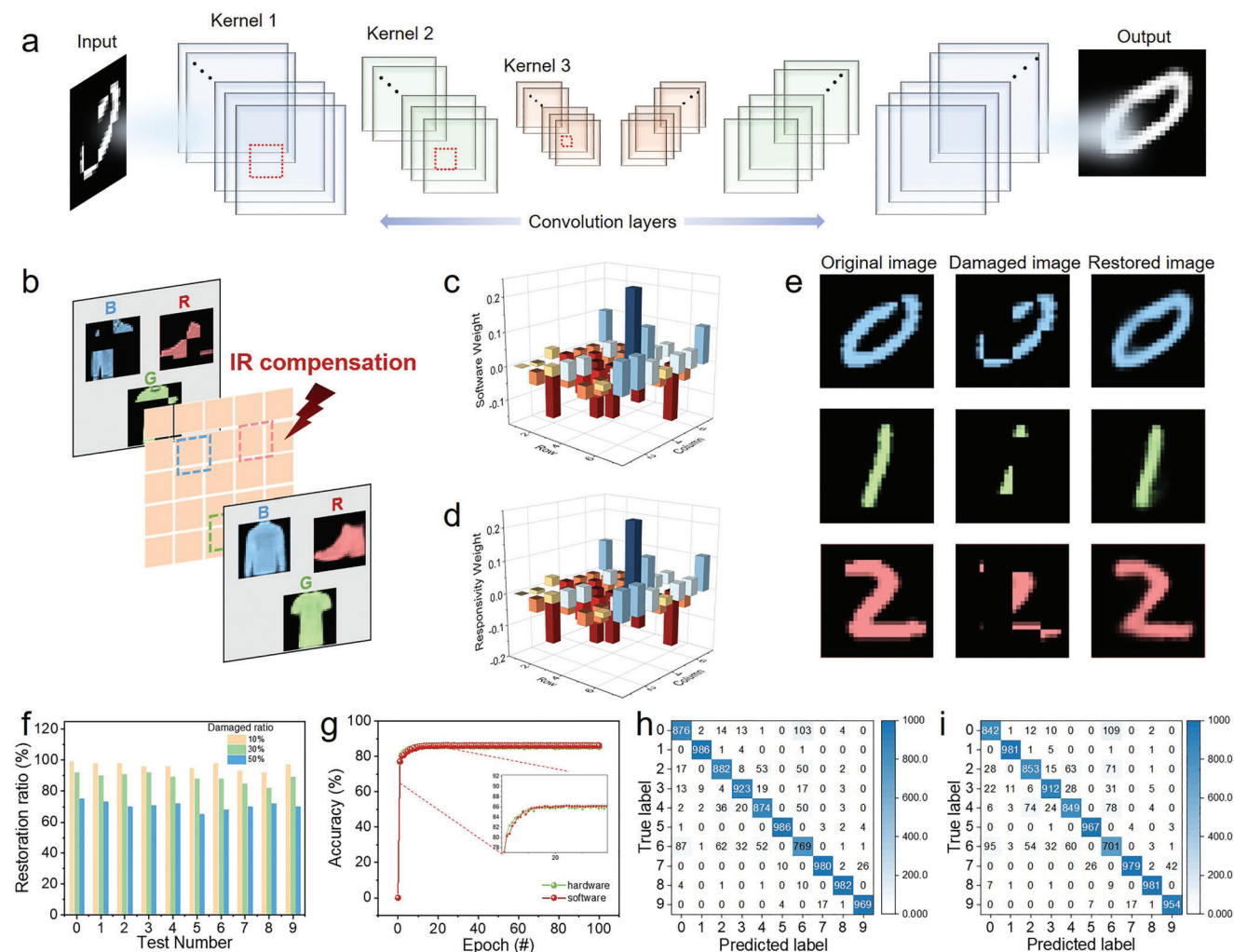
Figure 5. a) The CAE network used for image restoration. The network performs image restoration through a two-step process of encoder and decoder. b) Through IR light compensation, the phototransistor array can adaptively restore accurate images of different colors while simultaneously sensing. c) Representation of the software-trained weight and d) hardware responsivity weights (a kernel of 7 × 7 is shown as an example). e) The original, damaged, and CAE-recovered images from the MNIST dataset with blue, green, and red colors. f) Statistical restoration ratios of MNIST images. g) MNIST images restored by the CAE network, which uses software-trained and hardware responsivity weights. The restored images are evaluated using ResNet to determine recognition accuracy. The confusion matrix resulting from the recognition accuracy of MNIST images restored by the CAE network, utilizing h) software-trained weights and i) hardware responsivity weights. The confusion matrix is generated using ResNet for image classification, illustrating the performance of the restored images.

and S2, Supporting Information). Corresponding device weights were determined by linearly mapping the device's responsivity to trained weights. These trained weights are displayed in Figure 5c, and the linear responsivity mapping is shown in Figure 5d. Additionally, the weight errors for the 7 × 7 kernel were analyzed. To streamline weight adjustments within the neural network framework, the HDF5 file format in Python was employed, enabling direct modification of the pre-trained model's weight parameters. This approach seamlessly integrates the device's unique responsivity profile into the CAE network, enhancing its adaptability for accurate image processing. In addition to the blue light response, Figure S23 (Supporting Information) also shows the response weights at 532 and 635 nm wavelengths, while the corresponding response weights were also extracted and presented in Tables S3 and S4 (Supporting Information). The response to

1550 nm light is pivotal in complementing the device's response across visible wavelengths (450, 532, and 635 nm), enabling effective spectral compensation crucial for preserving image integrity and restoration accuracy. In scenarios where visible light data is impacted by noise, the device utilizes its broadband bidirectional photoresponse to perform convolutional processing on the image, facilitating comprehensive restoration through the CAE network. This approach allows the device to dynamically adjust its response based on the spectral features of the input light, thereby offering a resilient and adaptive solution for handling varied and challenging imaging conditions.

The adaptive restoration capability is demonstrated using a phototransistor array to restore damaged images successfully. The efficacy of the proposed method is shown through a series of experiments involving the MNIST dataset. In these

experiments, the original and damaged photos are presented in blue, green, and red color, respectively (Figure 5e). R-weight, G-weight, and B-weight were used to recover these damaged images, resulting in notable outcomes. This provides clear evidence of the network's ability to restore images with various forms of damage, bringing them closer to their original appearance. Effectively managing responses across different wavelengths highlights the device's advanced functionality in real-world imaging applications. Integrating IR and visible light responses underscores the device's effectiveness in adaptive image restoration. It is a valuable tool for applications requiring precise color reproduction and reliable data recovery across various spectral conditions.

To further confirm the performance of the CAE network, statistical restoration ratios for the MNIST images are presented in Figure 5f. The restoration ratios of images with varying degrees of damage were statistically analyzed using the device-specific weights within the CAE network. Even when each image was 50% damaged (as exemplified by the blue images), the restoration ratio remained above 65%. These ratios offer a comprehensive overview of the network's restoration efficiency, highlighting its capacity to recover the damaged image. The restored images are further evaluated using ResNet, a deep-learning model renowned for its image recognition capabilities. Using the blue digital image as the example, Figure S24 (Supporting Information) shows the damaged and restored results for digit images of 0–9. The comparison involves assessing the recognition accuracy of images restored using both software-trained weights and hardware responsivity weights in the CAE network (Figure 5g). The recognition accuracy for the digit images was 86.3% with software-trained weights and 85.8% with hardware responsivity weights in the CAE network. The results of this evaluation are depicted through confusion matrices (Figures 5h,i), which are generated using ResNet-based classification. These matrices provide a detailed analysis of the recognition accuracy, offering insights into the network's performance in accurately classifying the restored images. Additionally, to demonstrate the versatility of the CAE network utilizing PQDs/BP phototransistors, the same network was employed to reconstruct damaged Fashion MNIST dataset (Figure S25, Supporting Information). This application resulted in a high recognition accuracy of 81.7% (Figure S26, Supporting Information). The classifications' consistency and accuracy further demonstrate the CAE network's reliability, even when transitioning from software-trained models to hardware models. Table S5 (Supporting Information) highlights the unique capabilities of the developed device compared to previous in-sensor devices.[1,11,46,49–54] Photodetectors and neuromorphic sensors handle tasks with limited adaptability to lighting conditions. In contrast, our device integrates multi-spectral in-sensor convolution functionality, enabling operations across visible and infrared ranges. This dual capability supports both letter classification and advanced tasks like image segmentation and damaged image reconstruction, making it ideal for complex machine vision applications under varied lighting conditions. With exceptional responsiveness and in-sensor computing capabilities, the BP/PQDs phototransistor offers a promising pathway for developing systems with enhanced performance and functionality, particularly when combined with neural networks or diverse electronic components.

3. Conclusion

In conclusion, the biologically inspired adaptive broadband image sensor significantly improves image perception in complex lighting environments. Utilizing type-I band alignment between PQDs and BP, the sensor enables precise control of carrier injection and advanced real-time image processing. Its dual-mode response to visible and IR lights allows for selective enhancement and accurate feature extraction. With a restoration accuracy exceeding 85%, the sensor mitigates image quality degradation and provides a versatile solution for machine vision applications requiring adaptive imaging under varying lighting conditions.

Supporting Information

Supporting Information is available from the Wiley Online Library or from the author.

Conflict of Interest

The authors declare no conflict of interest.

Data Availability Statement

The data that support the findings of this study are available from the corresponding author upon reasonable request.

[1] L. Mennel, J. Symonowicz, S. Wachter, D. K. Polyushkin, A. J. Molina-Mendoza, T. Mueller, *Nature* **2020**, *579*, 62.

[2] L. Li, L. Shao, X. Liu, A. Gao, H. Wang, B. Zheng, G. Hou, K. Shehzad, L. Yu, F. Miao, Y. Shi, Y. Xu, X. Wang, *Nat. Nanotechnol.* **2020**, *15*, 743.

[3] S. Zang, M. Ding, D. Smith, P. Tyler, T. Rakotoarivelo, M. A. Kaafar, *IEEE Veh. Technol. Mag.* **2019**, *14*, 103.

[4] M. Jokela, M. Kutila, P. Pyykönen, *Appl. Sci.* **2019**, *9*, 2341.

[5] R. D. Jansen-van Vuuren, A. Armin, A. K. Pandey, P. L. Burn, P. Meredith, *Adv. Mater.* **2016**, *28*, 4766.

[6] M. Pan, Y. Fu, M. Zheng, H. Chen, Y. Zang, H. Duan, Q. Li, M. Qiu, Y. Hu, *Light Sci. Appl.* **2022**, *11*, 195.

[7] Z. Xu, X. Yuan, T. Zhou, L. Fang, *Light Sci. Appl.* **2022**, *11*, 255.

[8] C. Choi, H. Kim, J. H. Kang, M. K. Song, H. Yeon, C. S. Chang, J. M. Suh, J. Shin, K. Lu, B. I. Park, Y. Kim, H. E. Lee, D. Lee, J. Lee, I. Jang, S. Pang, K. Ryu, S. H. Bae, Y. Nie, H. S. Kum, M.-C. Park, S. Lee, H.-J. Kim, H. Wu, P. Lin, J. Kim, *Nat. Electron.* **2022**, *5*, 386.

[9] C. Choi, G. J. Lee, S. Chang, Y. M. Song, D. H. Kim, *ACS Nano* **2024**, *18*, 1241.

[10] F. Li, D. Li, C. Wang, G. Liu, R. Wang, H. Ren, Y. Tang, Y. Wang, Y. Chen, K. Liang, Q. Huang, M. Sawan, M. Qiu, H. Wang, B. Zhu, *Nat. Commun.* **2024**, *15*, 3689.

[11] Y. Yang, C. Pan, Y. Li, X. Yangdong, P. Wang, Z. A. Li, S. Wang, W. Yu, G. Liu, B. Cheng, Z. Di, S. J. Liang, F. Miao, *Nat. Electron.* **2024**, *7*, 225.

[12] B. Ouyang, J. Wang, G. Zeng, J. Yan, Y. Zhou, X. Jiang, B. Shao, B. Chai, *Nat. Electron.* **2024**, *7*, 705.

[13] M. Dong, Y. Zhang, J. Zhu, X. Zhu, J. Zhao, Q. Zhao, L. Sun, Y. Sun, F. Yang, W. Hu, *Adv. Mater.* **2024**, *36*, 2409550.

[14] B. H. Robison, K. R. Reisenbichler, *Copeia* **2008**, *2008*, 780.

[15] Y. Feng, Y. Zhang, Z. Zhou, P. Huang, L. Liu, X. Liu, J. Kang, *Nat. Commun.* **2024**, *15*, 1132.

[16] Z. Chen, Z. Lin, J. Yang, C. Chen, D. Liu, L. Shan, Y. Hu, T. Guo, H. Chen, *Nat. Commun.* **2024**, *15*, 1930.

[17] J. Xia, C. Gao, C. Peng, Y. Liu, P. A. Chen, H. Wei, L. Jiang, L. Liao, H. Chen, Y. Hu, *Nano Lett.* **2024**, *24*, 6673.

[18] M. Li, S. Peng, S. Fang, Y. Gong, D. Yang, K. Bu, B. Liu, H. Luo, S. Guo, J. Li, H. Wang, Y. Liu, S. Jiang, C. Lin, X. Lu, *J. Phys. Chem. Lett.* **2022**, *13*, 2555.

[19] S. Allard, M. Forster, B. Souharce, H. Thiem, U. Scherf, *Angew Chem. Int. Ed. Engl.* **2008**, *47*, 4070.

[20] T. Izawa, E. Miyazaki, K. Takimiya, *Adv. Mater.* **2008**, *20*, 3388.

[21] H. N. Tsao, D. Cho, J. W. Andreasen, A. Rouhanipour, D. W. Breiby, W. Pisula, K. Müllen, *Adv. Mater.* **2009**, *21*, 209.

[22] Y. Xu, H. Sun, W. Li, Y. F. Lin, F. Balestra, G. Ghibaudo, Y. Y. Noh, *Adv. Mater.* **2017**, *29*, 1702729.

[23] L. Protesescu, S. Yakunin, M. I. Bodnarchuk, F. Krieg, R. Caputo, C. H. Hendon, R. X. Yang, A. Walsh, M. V. Kovalenko, *Nano Lett.* **2015**, *15*, 3692.

[24] D. Li, B. Lyu, J. Sun, Q. Xiong, H. Zhu, Z. Jiang, D. Zhang, C. Liu, W. C. H. Choy, *ACS Energy Lett.* **2024**, *9*, 3261.

[25] H. Shao, Y. Li, W. Yang, X. He, L. Wang, J. Fu, M. Fu, H. Ling, P. Gkoupidenis, F. Yan, L. Xie, W. Huang, *Adv. Mater.* **2023**, *35*, 2208497.

[26] B. Lyu, D. Li, Q. Wang, J. Sun, Q. Xiong, D. Zhang, H. Su, W. C. H. Choy, *Angew Chem. Int. Ed. Engl.* **2024**, *136*, 202408726.

[27] W. J. Mir, A. Alamoudi, J. Yin, K. E. Yorov, P. Maity, R. Naphade, B. Shao, J. Wang, M. N. Lintangpradipto, S. Nematulloev, A. H. Emwas, A. Genovese, O. F. Mohammed, O. M. Bakr, *J. Am. Chem. Soc.* **2022**, *144*, 13302.

[28] H. Yoshimura, M. Yamauchi, S. Masuo, *J. Phys. Chem. Lett.* **2020**, *11*, 530.

[29] J. Hu, C. Bi, K. Ren, X. Zhang, W. Wang, S. Ma, M. Wei, Y. Lu, M. Sui, *Nano Lett.* **2024**, *24*, 4571.

[30] X. Zou, Y. Li, G. Tang, P. You, F. Yan, *Small* **2019**, *15*, 1901004.

[31] Q. Zhou, H. Zhou, W. Tao, Y. Zheng, Y. Chen, H. Zhu, *Nano Lett.* **2020**, *20*, 8212.

[32] J. Zhang, T. Zhang, Z. Ma, F. Yuan, X. Zhou, H. Wang, Z. Liu, J. Qing, H. Chen, X. Li, S. Su, J. Xie, Z. Shi, L. Hou, C. Shan, *Adv. Mater.* **2023**, *35*, 2209002.

[33] H. Funk, O. Shargaieva, A. Eljarrat, E. L. Unger, C. T. Koch, D. Abou-Ras, *J. Phys. Chem. Lett.* **2020**, *11*, 4945.

[34] X. Huang, Q. Li, W. Shi, K. Liu, Y. Zhang, Y. Liu, X. Wei, Z. Zhao, Y. Guo, Y. Liu, *Small* **2021**, *17*, 2102820.

[35] W. Wang, X. X. Li, T. Wang, W. Huang, Z. G. Ji, D. W. Zhang, H. L. Lu, *IEEE Trans. Electron Devices* **2020**, *67*, 3141.

[36] X. Chen, X. Lu, B. Deng, O. Sinai, Y. Shao, C. Li, S. Yuan, V. Tran, K. Watanabe, T. Taniguchi, D. Naveh, L. Yang, F. Xia, *Nat. Commun.* **2017**, *8*, 1672.

[37] Y. Xu, C. Liu, C. Guo, Q. Yu, W. Guo, W. Lu, X. Chen, L. Wang, K. Zhang, *Nano Energy* **2020**, *70*, 104518.

[38] S. Subramanian Periyal, M. Jagadeeswararao, S. E. Ng, R. A. John, N. Mathews, *Adv. Mater. Technol.* **2020**, *5*, 2000514.

[39] J. Gong, H. Yu, X. Zhou, H. Wei, M. Ma, H. Han, S. Zhang, Y. Ni, Y. Li, W. Xu, *Adv. Funct. Mater.* **2020**, *30*, 2005413.

[40] H. Y. Hou, S. Tian, H. R. Ge, J. D. Chen, Y. Q. Li, J. X. Tang, *Adv. Funct. Mater.* **2022**, *32*, 2209324.

[41] C. Han, X. Liu, X. Han, M. He, J. Han, H. Zhang, X. Hou, H. Zhou, H. Yu, Z. Wu, J. Gou, J. Wang, *Adv. Funct. Mater.* **2022**, *32*, 2209680.

[42] Y. Chen, Y. Kang, H. Hao, X. Xie, J. Zeng, T. Xu, C. Li, Y. Tan, L. Fang, *Adv. Funct. Mater.* **2022**, *33*, 2209781.

[43] X. Huang, Y. Liu, G. Liu, K. Liu, X. Wei, M. Zhu, W. Wen, Z. Zhao, Y. Guo, Y. Liu, *Adv. Funct. Mater.* **2022**, *33*, 2208836.

[44] X. Chen, B. Chen, B. Jiang, T. Gao, G. Shang, S. T. Han, C. C. Kuo, V. A. L. Roy, Y. Zhou, *Adv. Funct. Mater.* **2022**, *33*, 2208807.

[45] X. Feng, L. Gao, *Na.t Commun* **2021**, *12*, 2179.

[46] L. Pi, L. Wang, S. J. Liang, P. Luo, H. Wang, D. Li, Z. Li, P. Chen, X. Zhou, F. Miao, T. Zhai, *Nat. Electron.* **2022**, *5*, 248.

[47] D. Hu, Y. Zhang, J. Liu, S. Luo, Y. Chen, *IEEE Trans. Med. Imaging* **2022**, *41*, 1778.

[48] M. Weigert, U. Schmidt, T. Boothe, A. Muller, A. Dibrov, A. Jain, B. Wilhelm, D. Schmidt, C. Broaddus, S. Culley, M. Rocha-Martins, F. Segovia-Miranda, C. Norden, R. Henriques, M. Zerial, M. Solimena, J. Rink, P. Tomancak, L. Royer, F. Jug, E. W. Myers, *Nat. Methods* **2018**, *15*, 1090.

[49] J. Meng, T. Wang, H. Zhu, L. Ji, W. Bao, P. Zhou, L. Chen, Q. Q. Sun, D. W. Zhang, *Nano Lett.* **2022**, *22*, 81.

[50] L. Xu, J. Liu, X. Guo, S. Liu, X. Lai, J. Wang, M. Yu, Z. Xie, H. Peng, X. Zou, X. Wang, R. Huang, M. He, *Nat. Commun.* **2024**, *15*, 9011.

[51] X. Pang, Y. Wang, Y. Zhu, Z. Zhang, D. Xiang, X. Ge, H. Wu, Y. Jiang, Z. Liu, X. Liu, C. Liu, W. Hu, P. Zhou, *Nat. Commun.* **2024**, *15*, 1613.

[52] J. Fu, C. Nie, F. Sun, G. Li, H. Shi, X. Wei, *Sci. Adv. 10*, **2024**, eadk8199.

[53] Y. Zhu, Y. Wang, X. Pang, Y. Jiang, X. Liu, Q. Li, Z. Wang, C. Liu, W. Hu, P. Zhou, *Nat. Commun.* **2024**, *15*, 6015.

[54] G. X. Zhang, Z. C. Zhang, X. D. Chen, L. Kang, Y. Li, F. D. Wang, L. Shi, K. Shi, Z. B. Liu, J. G. Tian, J. Zhang, *Sci. Adv.* **2023**, *9*, eadi5104.